Nanoscale

PAPER

View Article Online
View Journal | View Issue

Cite this: *Nanoscale*, 2025, **17**, 2528

Multipurpose triadic MXene/garlic/gellan gum-based architecture in the horizon of bone tissue regeneration

Lin Zhou,†[a] Zhuo Zhao,†[b] Seyedeh Nooshin Banitaba,[c] Sanaz Khademolqorani,[c] Xin Han *[a] and Guang Chen *[a]

The use of bioresorbable compositions has been considered a promising therapeutic approach for treating compromised bone tissues. Gellan gum (GG) is a predominant polysaccharide recognized for its exceptional biocompatibility and biodegradability, facile bio-fabrication, and customizable mechanical attributes, rendering it well-suited for developing versatile bone scaffolds. On the other hand, MXene nanosheets have been declared a representational filler to augment the osteogenic effect and amend the mechanical properties of the polymeric biomaterials. Herein, the GG/MXene system was formulated to investigate the synergistic impact of gellan gum and MXene on promoting bone tissue engineering. Accordingly, $Ti_3C_2T_x$ MXene nanogalleries were synthesized and loaded with 1, 3, and 5 wt% ratios into the GG matrix to fortify the overall performances. Based on the outcomes, the GG containing 1 wt% MXene showed a homogeneous surface with an optimized topography, providing greater amorphous regions (15%), boosted hydrophilicity (27.5°), and a favorable Young's modulus (13.43 MPa). Additionally, the designed scaffold provided exceptional osteogenetic adhesion and bactericidal behavior against both Gram-positive (*S. aureus*) and -negative (*E. coli*) bacteria. To achieve more desirable biological performance, 1 ml garlic extract (GA) was introduced to the freeze-dried composite network. The results exhibited better cell attachment in the porous GA-mediated scaffold with furthered antibacterial features through an increase in the zone diameter breakpoint from 4.8 ± 0.2 and 5.0 ± 0.1 mm to 5.9 ± 0.3 and 6.2 ± 0.2 mm against *S. aureus* and *E. coli*, respectively. Therefore, embedding GA, alongside MXene layered nanomaterials, into the GG-based matrix could provide a convenient scaffolding architecture for guided bone regeneration, facilitating appropriate cell attachment, growth, and proliferation.

Received 29th September 2024,
Accepted 17th December 2024

DOI: 10.1039/d4nr03995e

rsc.li/nanoscale

1. Introduction

Tissue engineering is a field of regenerative medicine that seeks to repair or replace living tissues using well-designed tissue mimics. Hard tissues, such as bone, consist primarily of calcified structures rich in calcium phosphate minerals. Common orthopedic issues like bone defects can cause significant damage, leading to high-risk operations and surgeries requiring prolonged treatment. With an expected 25% increase in osteoporotic fractures between 2019 and 2034 due to an aging population, developing appropriate scaffolds has become crucial to aid the implantation process. Consequently, treating bone defects remains a significant challenge in clinical practice.[1]

The bone matrix is characterized by cancellous or spongy bone tissue enveloped by a compact outer boundary. It is conceivable that tailoring a suitable structure effectively imitates the intricate 3D native tissues.[2] In this regard, film and sponge-like fabricated architectures have provided appropriate bone tissue engineering conditions. So far, numerous endeavors have been devoted to fabricating versatile composites as bone scaffolds using synthetic or bio-based polymer matrixes.[3] In the virtue of green and eco-friendly polymers, Chang *et al.*[4] established that the gellan gum (GG) polysaccharide could exhibit significant promise for application in guided bone regeneration. The study revealed a positive correlation between tensile strength and film thickness. Moreover, histological assessment demonstrated the superior integrity of the GG film

[a]*Department of Orthopedic Surgery, The Second Hospital of Dalian Medical University, No. 467, Zhongshan Road, Shahekou District, Dalian City, Liaoning 116021, China. E-mail: hanxin1973@163.com, chenguang987123@126.com*
[b]*Department of Hands and Feet Microsurgery, The Second Hospital of Dalian Medical University, Liaoning 116021, China*
[c]*Emerald Experts laboratory, Isfahan Science and Technology Town, Isfahan 84156-83111, Iran*
† Lin Zhou and Zhuo Zhao have contributed equally to this work and share first authorship.

in bone defect healing after 2 months, along with its favorable cell separation capability. Afterward, the merits of this outstanding polymer for generating bone scaffolds were declared in different architectural compositions through conducting numerous studies.[5,6] Accordingly, the tunability of the GG-based network is attainable through the variation of key parameters, including pH conditions, stabilization time, and freezing conditions, providing the opportunity to mimic bone grafting.[7]

The introduction of electroconductive fillers into the polymeric biomaterials has been accounted for as a recent development to augment the scaffolding features through boosting cell proliferation and differentiation by replicating the electrical characteristics of the native tissues.[8,9] As a representational electroconductive filler, the MXene family has emerged as a focal point in the current research activities. The layered MXene structure has enabled extensive utility in biomedical applications owing to its substantial surface area, compelling hydrophilicity, and antibacterial features. Accordingly, the literature suggests that loading MXenes into the polymeric structures may augment and potentiate the differentiation capacity of osteogenic cells and engender heightened alkaline phosphatase activity, thereby contributing to more efficient bone repair.[10] Due to the rich electronic properties of MXenes, these materials possess the capability to eliminate bacteria through the generation of cytotoxic reactive oxygen species (ROS) and oxidative stress upon photoexcitation.[11] Furthermore, the plentiful functional groups and hydrophilic nature of MXene nanosheets amplify their affinity with bacteria, while their razor-sharp edges have the potential to dismantle bacterial cell walls. As an example, Jang *et al.*[12] implied that employing Ti_3C_2 MXene with a concentration lower than 20 μg ml^{-1} could positively promote osteogenic differentiation. Additionally, it was observed that MXene effectively aids in the expression of early and late osteogenic genes. In another study, Zhao *et al.*[13] investigated the role of Ti_3C_2 MXene in the performance of gelatin-based scaffolds in ROS-scavenging and osteogenic capability. The MXene-loaded gelatin-based hydrogels exhibited exceptional compressive strength ranging from 44 to 75.6 kPa, along with a modulus of 24 to 44.5 kPa. Moreover, these hydrogels demonstrated the capacity to scavenge ROS, specifically –OH and DPPH radicals, thereby safeguarding MC3T3-E1 cells from oxidative stress. Notably, the integrated structure with the MXene nanomaterial displayed non-toxic attributes toward MC3T3-E1 cells, boosted alkaline phosphatase secretion and calcium nodule formation, and upregulated osteogenic gene expression.

It is worth mentioning that infection poses a significant challenge during the bone repair process. When grafts are used, especially in open fractures, the risk of developing a bone infection increases considerably. This issue arises from colonizing harmful bacteria and fungi in the wound. Staphylococcus bacteria (*S. aureus*) and *Escherichia coli* (*E. coli*) are the primary agents responsible for these infections. Accordingly, it is crucial to address this challenge, as untreated bone infections can lead to graft failure, jeopardizing recovery and overall health.[14] Regarding the MXene-loaded scaffolds, the impact of MXene on bacterial loss and cell survival rate is deeply dependent on the MXene concentration. Therefore, favorable biological outcomes could only be approached through embedding MXene below the optimized range, requiring the incorporation of appropriate additives.[8] In this era, garlic extract (GA) has exhibited notable antibacterial properties owing to its sulfur-containing phytochemicals. GA has demonstrated excellent antibacterial and osteogenic activities, particularly in the context of bone tissue engineering.[15] Bose *et al.*[16] developed a garlic/bioceramics composite for bone regeneration, corroborating the establishment of a pro-osteogenic environment through the release of garlic extract, as evidenced by a fourfold increase in phosphatase activity. In light of these data, we seize a composition platform to engineer and optimize versatile bone tissue engineering through homogeneous distribution of $Ti_3C_2T_x$ MXene and GA in a highly porous GG-based polymeric network. Considering the characteristics attributed to each component, the developed architecture is expected to bring outstanding mechanical and biological properties that will mimic the native bone extracellular matrix, thereby proposing a promising composition for bone tissue engineering and other biomedical domains.

2. Materials and methods

2.1 Synthesis of MXene nanosheets

The production of layered $Ti_3C_2T_x$ MXene nanosheets was initiated *via* the etching progress of the commercially available Ti_3AlC_2 powder (Sigma Aldrich Co., USA), with a purity of 90.0% and a particle size of 100 mesh. Primarily, 2 g Ti_3AlC_2 powder was dispersed in 20 ml of 50% w/v HF solution and vigorously stirred at 50 °C for a duration of 48 h in an oil bath environment. Subsequently, the resulting solution was washed multiple times with distilled water (DI) using a centrifuge operating at 4000 rpm until the pH approached 6. The prepared powder was combined with 50 ml of DI, to which 40 ml of dimethyl sulfoxide was introduced. The solution was continuously stirred for 24 h, ultimately resulting in the synthesis of exfoliated MXene nanosheets through vacuum filtration and subsequent drying.

2.2 Preparation of MXene-loaded polymeric layers

0.166 g of gellan gum low acyl (GELZAN™ CM, G1910, Sigma Aldrich) was added to 10 ml of DI as a solvent and stirred for 4 h at 100 °C to prepare a homogeneous transparent solution. Based on trial and error and in line with the attempts carried out by Razali *et al.*[17] and Ismail *et al.*,[18] 0.0833 g glycerin was also introduced to approach a homogeneous solution. Simultaneously, the mixtures of MXene/DI with concentrations of 1, 3, and 5 wt% were prepared and stirred for 12 h at ambient temperature. Next, the sonicated MXene solution at 50 Hz for 10 min was introduced into the obtained gellan gum solution and stirred for 5 h. Finally, the solutions were poured into Petri dishes and left to dry in the air. The obtained

matrixes containing 0, 1, 3, and 5 wt% MXene nanogalleries were coded as Pure GG, GG@1#$Ti_3C_2T_x$, GG@3#$Ti_3C_2T_x$, and GG@5#$Ti_3C_2T_x$, respectively.

The garlic extract was also produced according to patent NO. CN101863807A, involving the following steps: peeling, washing, and slicing garlic, soaking it in water, and then filtering it with a 50–100-mesh sieve to obtain a garlic extract solution. Subsequently, the garlic extract solution was distilled under reduced pressure. During this process, sodium hydroxide was added to the distillate to adjust the pH value to 9–14, and the mixture was left to stand for 5–20 min at room temperature. Finally, hydrochloric acid was added for neutralization. To prepare the samples containing the garlic extract, 1 and 3 ml of the attained garlic extract solution was added to GG@1#$Ti_3C_2T_x$, mixed for 12 h, sonicated for 12 h, and finally cast. An additional freeze-drying step was also used to create porosity in the modified scaffold loaded with garlic extract. Accordingly, gel samples were frozen at −18 °C for 24 h and then placed in a freeze dryer at room temperature for 48 h. The drying process was performed at a chamber pressure of 0.18 mbar and a condenser temperature of −110 °C. Upon completion of the drying process, the samples were carefully placed in a desiccator containing silica gel beads under low-vacuum conditions to prepare them for characterization.

2.3 Physiochemical characterization of the cast matrixes

The fascinating morphological characteristics of the $Ti_3C_2T_x$ nanosheets and the prepared compositions were meticulously examined using a state-of-the-art field emission scanning electron microscope (FESEM, NOVA NANOSEM 230, Philips) operating at an accelerating voltage of 5 kV and fortified with EDS mapping. The surface roughness of the generated films was evaluated using atomic force microscopy (AFM, JPK, NanowizardII) under normal conditions. High-quality images were obtained as an outcome of this analysis, revealing average roughness in specimens. Furthermore, we employed the powerful attenuated total reflectance (ATR) Fourier-transform infrared spectroscopy (FTIR, BOMEM-MB100) to capture the FTIR spectra of the designed membranes across a broad wavelength range from 4000 to 400 cm^{-1}. Lastly, the crystalline structure of the architectures was unveiled using an advanced X-ray diffractometer (Philips X'pert MPD) within an angle range (2θ) from 10 to 90° with a step size of 0.1°. The Scherrer equation (eqn (1)) and Bragg Law (eqn (2)) were utilized to estimate the crystal size (τ) and spacing between the crystal parts (d) in the MXene nanosheets. In the equations, K, λ, β, θ, and n are denoted as the shape factors (≈1), X-ray wavelength (≈0.154 nm), the extended line at half maximum intensity of the peak, incident angle, and diffraction order (≈1), respectively.

$$\tau = \frac{K\lambda}{\beta \cos \theta} \quad (1)$$

$$d = \frac{n\lambda}{2 \cdot \sin \theta} \quad (2)$$

Using the XRD patterns, the crystalline regions in the specimens were identified *via* the following formula (eqn (3)):

$$X_C\,(\%) = \frac{\text{The area under the crystalline peaks}}{\text{The area under total peaks}} \times 100 \quad (3)$$

A standard sessile drop method was also employed to assess the contact angle and so hydrophilicity of the membranes. DI (1 μl) was precisely released on the surfaces of the scaffolds and then captured employing a digital camera. The results were evaluated using the Image J tool (National Institutes of Health, Bethesda, MD). Based on the data, the average contact angles, spreading coefficient, and work of adhesion were calculated by the specified equations (eqn (4)–(6)), respectively.

$$\cos \theta = \frac{\gamma_{m/a} - \gamma_{m/l}}{\gamma_{l/a}} \quad (4)$$

In the formula above, the contact angle (θ) denotes the angle formed by a liquid droplet on the surface of a membrane. In addition, the surface tensions between the membrane/air, membrane/liquid, and liquid/air interfaces are signified by $\gamma_{m/a}$, $\gamma_{m/l}$, and $\gamma_{l/a}$, respectively.

$$S = \sigma_f - \sigma_d - \sigma_{df} \quad (5)$$

The spreading coefficient (S) is the disparity between the surface tension of the foaming medium (σ_f), the surface tension of the defoamer (σ_d), and the interfacial tension between materials (σ_{df}).

$$W_a = \gamma_L - \gamma_S - \gamma_{SL} \quad (6)$$

In eqn (6), γ_L and γ_S indicate the surface energy (tension) of the liquid and the solid phases, respectively. γ_{SL} and W_a also symbolize the interfacial surface tension and the work of adhesion.

2.4 Thermal analysis

The thermal stability of the cast films was analyzed using a cutting-edge thermogravimetric analyzer (NETZSCH STA 449F3). The investigation entailed heating the samples from 25 to 600 °C at a ramping rate of 10 °C min^{-1} under an inert atmosphere (N_2). Additionally, differential scanning calorimetry (DSC) was conducted to glean comprehensive insights into the thermal stability of the specimens.

2.5 Uniaxial mechanical strength and cyclic test

The remarkable tensile properties of the fabricated films were analyzed using a Zwick/Roell machine (Z010, Germany). Precision-cut specimens, each measuring 5 cm × 0.5 cm, underwent thorough examination at a machine speed of 0.5 cm min^{-1}, with a load cell of 20 N, and an initial length of 3 cm. The thickness of the samples was determined using a digital micrometer (Insize non-rotating spindle digital micrometer 3631-25, China). To ensure robust and reliable results, each sample was rigorously tested thrice at ambient temperature and 65% humidity. For loading-unloading tests, a

detailed analysis was conducted focusing on the maximum strain exhibited by the membranes. The loading and unloading procedures were continued for up to 30 cycles to evaluate the material's response to repeated stress conditions thoroughly.

2.6 Swelling behavior and degradation analysis

The swelling ratio of the samples was examined by immersing them in DI. Accordingly, the samples were weighed before subjection to DI and at various time intervals after immersion for 48 hours. Then, the Swelling % = ((Wet wight − dried weight)/dried weight) × 100 formula was utilized to calculate the swelling ratio in specimens. To observe the degradation behavior, all samples were carefully weighed and subsequently immersed in a phosphate-buffered saline (PBS) solution designed to simulate the human body's environment (pH ~ 7). Throughout the experiment, the three specimens were regularly retrieved from the solution and rinsed with distilled water to remove any degradation products or residual impurities. Following this rinsing process, the samples were dried in an incubator at 60 °C for 12 h. Once the drying process was completed, the samples were weighed again. Finally, the remaining weight plot was provided to display the degradation rate of the samples with the passing time.

2.7 Antibacterial test

The antibacterial properties of the fabricated structures were tested against both *S. aureus* Gram-positive and *E. coli* Gram-negative bacteria. The antibiogram analysis was conducted following the ISO protocol (No. 20776-1:2006). The process kicked off with a 24 h bacteria cultivation at 35 ± 2 °C in a liquid medium. Next up, a specific volume of the bacterial suspension was carefully placed on a solid culture medium to encourage colony isolation. The isolated bacterial colonies were then pampered in sterile serum to achieve a final concentration of 0.5 McFarland. The resulting bacterial solution was affectionately spread using a sterilized swab and placed on a microbial solid culture medium for a cozy incubation. The crafted specimens were then introduced into the prepared medium and given a warm 24-hour incubation at 37 °C. Finally, the growth area was thoroughly evaluated, providing a wealth of data on the antibacterial properties of the tested structures.

2.8 Cell viability assay

The cytotoxicity of the developed scaffolds was examined using the Osteosarcoma MG63 cell line. We cultured 5×10^4 MG63 cells in Dulbecco's Modified Eagle's Medium (DMEM, Solarbio, China) with 10% fetal bovine serum (FBS, Gibco, China), as well as 1% penicillin and streptomycin. The experiment involved adding samples weighing 1.0 ± 0.1 mg, with n = 3, to a 24-well plate and then placing the plate in an incubator with 5% CO_2 at 37 ± 1 °C for 24 ± 2 h. Afterward, 100 μl of MTT dye with a 5 mg ml^{-1} concentration was added to the cell culture well plates. After 3 h, the MTT dye was removed, and DMSO solvent was added to ensure the complete dissolution of the formed purple crystals. We then quantified the dissolved dye in the DMSO solvent using an ELISA device, with living cells exhibiting a higher optical density (OD) than dead cells. The attained results allowed the estimation of the cell viability ratio using the following formula (eqn (7)):

$$\text{Cell viability}\,(\%) = \frac{\text{OD average in sample}}{\text{OD average in control}} \times 100 \qquad (7)$$

2.9 Cell adhesion

The process of evaluating cells adhering to the provided scaffolds was initiated by sterilizing the samples using UV light. Subsequently, 5×10^4 MG63 cells cultured in DMEM (with 10% FBS, 1% penicillin, and streptomycin) were seeded into a 12-well plate encompassing the synthesized scaffolds. The plates were then incubated with 5% CO_2 at 37 ± 1 °C for 24 h. After the incubation period, the compositions were delicately washed with a phosphate buffer, ensuring the utmost care for the cells. Following this, the cells were expertly fixed using a specialized glutaraldehyde solution, guaranteeing precise and reliable results. The samples were then exposed to various concentrations of ethanol solutions (40, 50, 70, 95, and 100%), subsequently dried at 25 °C, coated with gold, and investigated by FESEM.

2.10 Statistical analysis

The recorded measurements from various experiments were replicated thrice to enable data representation as average ± std. Analysis *via* one-way ANOVA was employed to determine the differences between the obtained values, considering $P < 0.05$ to denote statistical significance.

3. Results and discussion

3.1 Morphological features of the synthesized MXene nanoflakes

MXene 2D nanoflakes were synthesized to integrate the mechanical and biological behavior of gellan gum-based bone tissues. The synthesis of 2D MXene flakes entailed exfoliating the Ti_3AlC_2 precursor, which was succeeded by an acidic treatment procedure applied to the layered structure of the MAX phase. Based on this, the Al element was selectively etched using hydrofluoric acid, causing the formation of a dynamic interaction between the fluoride ions and other components in the structure and, thereby, the generation of $Ti_3C_2T_x$ nanoflakes. In the chemical formula, T_x corresponds to the –F, –O, or –OH functional groups in the nanosheets. Fig. 1a–c represents the chemical structure and FESEM images of the attained MXene nanosheets. As is observable, a layered architecture was created, which could be assigned to the more stabilized linkage of M–X than the M–A and, therefore, successful M–A removal. An expansion occurred in the $Ti_3C_2T_x$ structure due to the weakening of the binding force between nanosheets through using dimethyl sulfoxide organic molecules, followed by an ultrasonication procedure. Elemental

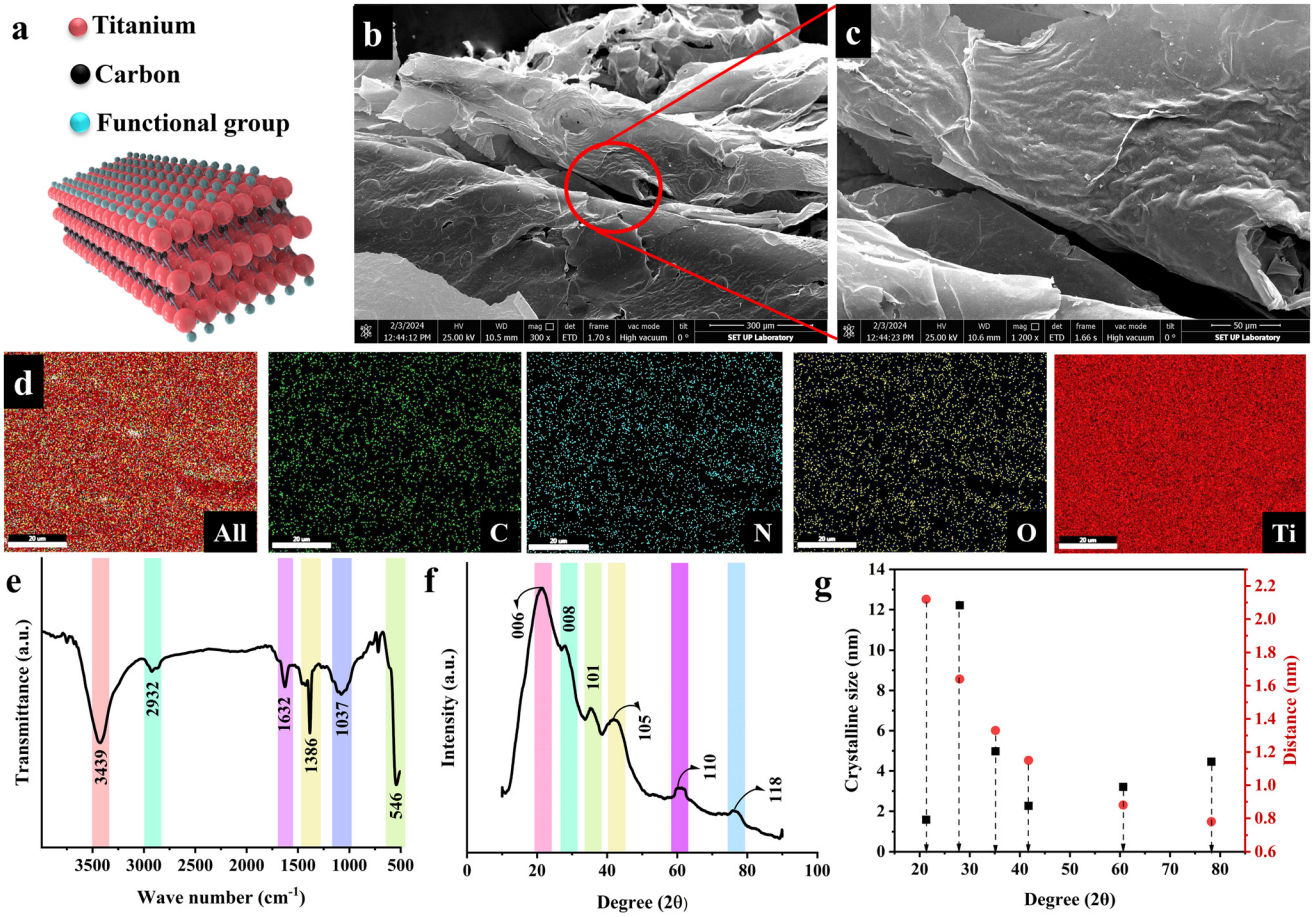

Fig. 1 Characteristics of the synthesized MXene nanosheets; (a) schematic illustration of the chemical structure, (b and c) FESEM images with various magnifications, (d) EDS mapping, (e) ATR-FTIR spectrum, (f) XRD pattern, and (g) the size and distance of crystal planes.

mapping of the synthesized MXene nanoflakes is shown in Fig. 1d, proving the uniform distribution of C, N, O, and Ti elements with weight ratios of 7.02, 0.45, 13.88, and 78.43% and atomic ratios of 17.24, 1.04, 28.33, and 53.45% in $Ti_3C_2T_x$, respectively. It is worth noting that, besides the observed prominent peaks in the synthesized structure, an extremely weak peak belonging to the remaining Al element was also observed, showing a 0.22% weight ratio and 0.54% atomic percentage. Based on the literature, the O element directly declares the presence of hydroxyl (–OH) and carboxyl (–COOH) functional groups.[19]

Fig. 1e also presents the ATR-FTIR analysis of MXene nanosheets. The obtained spectrum displays several characteristic peaks, showing the successful synthesis of the $Ti_3C_2T_x$ structure. The vibration mode observable at 3439 cm^{-1} is attributed to the –OH stretching, possibly due to atmospheric moisture in the synthesized MXene. The 2932 and 1632 cm^{-1} peaks also corresponded to C–H and C═O stretching peaks, respectively. Furthermore, the peaks at 1386, 1073, and 546 cm^{-1} could be attributed to the C–O, C–N, and Ti–O bands. The XRD diffraction pattern of the generated MXene nanoflakes is shown in Fig. 1f. In the recorded pattern, several peaks appeared, displaying the crystal planes of 006 (~21°), 008 (~28°), 101 (~35°), 105 (~41°), 110 (~60°), and 118 (~76°). The successful $Ti_3C_2T_x$ synthesis could be proved by the formation of 006 and 008 crystal planes. The crystal plane observed at 28° might be related to the existence of water between the MXene nanosheets and the formation of $Ti_3C_2(OH)_2$. The feeble peaks linked to the 101 and 105 crystal planes also corresponded to the TiC impurity created during the synthesis. It is worth noting that the aluminum characteristic peak appears at 39°, which was absent in the obtained spectrum, declaring the complete Ti_3AlC_2 etching in the employed synthesis route. Fig. 1g provides the size and distance of the $Ti_3C_2T_x$ crystalline planes, estimated through Scherrer equation and Bragg's law, respectively. Accordingly, the 006, 008, 101, 105, 110, and 118 crystal planes exhibited the size of 1.58, 12.22, 4.98, 2.27, 3.21, and 4.47 nm with crystal distances of 2.12, 1.64, 1.33, 1.15, 0.88, and 0.78 nm. The obtained data approved the creation of fine $Ti_3C_2T_x$ MXene sheets in the nanoscale range.

3.2 Physiochemical characteristics of the generated polymeric scaffolds

The utilized method for synthesizing polymeric scaffolds, along with the FESEM and AFM images of the resulting mem-

branes, encompassing Pure GG, GG@1#$Ti_3C_2T_x$, GG@3#$Ti_3C_2T_x$, and GG@5#$Ti_3C_2T_x$, are portrayed in Fig. 2a. The polymeric film exhibited a surface structure characterized by homogeneity and roughness, indicative of the presence of MXene spherulites within the composition. It seems that during the film formation procedure, the MXene structure underwent reconfiguration, assuming jelly-like formations within the gellan gum and giving rise to microspheres on the surface. Detailed analyses revealed that an increase in the MXene content from 1 to 3 wt% led to a reduction in the microsphere diameter from 6.3 ± 5.8 to 4.8 ± 2.1 μm, while an increase in the MXene concentration up to 5 wt% facilitated the internal connectivity and enhanced an overall diameter expansion to 13.1 ± 7.7 μm. This transformation of MXene induced a conversion from a smooth and uniform surface to a rough texture in the gellan gum matrix.

The inclusion of MXene nanosheets within the composite structure disrupted the alignment of the closely packed

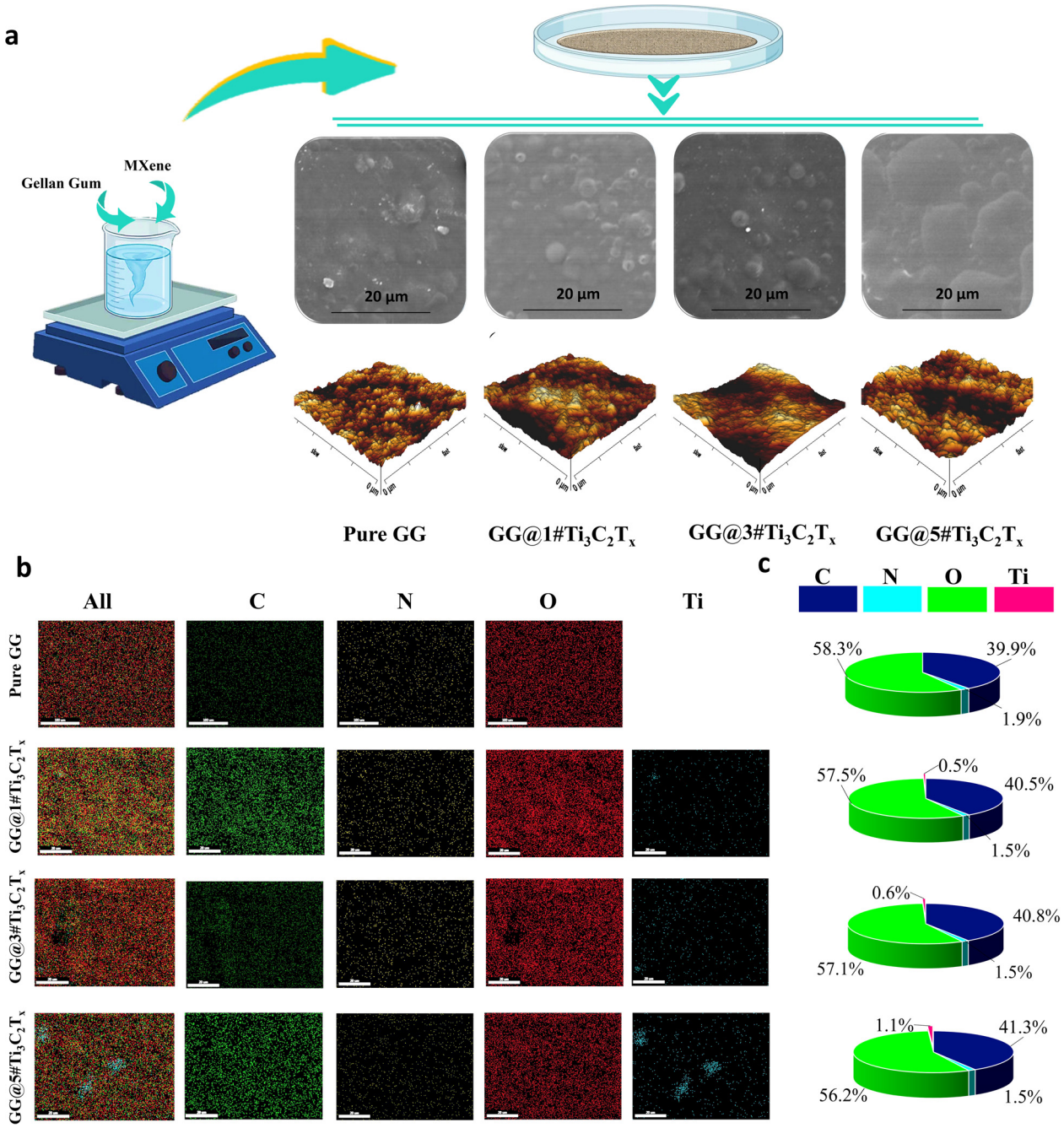

Fig. 2 Morphological features of the solution cast scaffolds; (a) FESEM images and AFM images recorded from the surface of the designed scaffolds, (b) EDS mapping, and (c) the percentages of C, N, O, and Ti elements presented in EDS map images of Pure GG, GG@1#$Ti_3C_2T_x$, GG@3#$Ti_3C_2T_x$, and GG@5#$Ti_3C_2T_x$ scaffolds.

polymer chains, potentially because of the formation of densely packed and overlapping phases by the $Ti_3C_2T_x$ nanoflakes. Furthermore, the remarkable surface-to-volume ratio of the $Ti_3C_2T_x$ element, combined with an increase in its concentration, was likely to generate a more extensive interfacial area with polymer phases. This, in turn, enhanced the composite density during the solidification process, ultimately impacting the resulting rugged surface topography. The topography of a substrate significantly impacts cell adhesion and proliferation, playing a crucial role in the rational design of bio-adhesives, tissue engineering, and the development of *in vitro* screening assays. The literature underscores the pivotal role of nano-geometry in facilitating stable cell adhesion and growth, indicating that moderately rough substrates may selectively enhance cell proliferation.[20,21] The images obtained from the AFM analysis approved the observed changes in the surface topography of the fabricated structures. Based on the attained data, the average roughness of 12.34, 33.19, 19.58, and 16.51 nm were obtained for Pure GG, GG@1#$Ti_3C_2T_x$, GG@3#$Ti_3C_2T_x$, and GG@5#$Ti_3C_2T_x$, respectively. Accordingly, a low ratio of MXene in the gellan gum structure could remarkably enhance the surface roughness. In contrast, the MXene content exceeding 5 wt% could form a smoother surface, perhaps due to the overlapping of the nanosheets.

Fig. 2b and c show the EDS mapping of the Pure GG, GG@1#$Ti_3C_2T_x$, GG@3#$Ti_3C_2T_x$, and GG@5#$Ti_3C_2T_x$, asserting the Ti, C, N, and O presence in the structures. Accordingly, the provided polymeric networks were composed of carbon, oxygen, and nitrogen elements in the proportions of 40, 57, and 1.5%, respectively, due to the chemical makeup of the gellan gum polymer and the presence of carbon in the MXene structure. In the film-cast architectures containing MXene nano galleries, the percentage of titanium increased from 0.5 to 1.1% as the amount of MXene in the structure upsurges. The EDS results clearly demonstrated a homogeneous distribution of compositional elements in Pure GG, as well as in GG@1#$Ti_3C_2T_x$ and GG@3#$Ti_3C_2T_x$, highlighting the consistent allocation of MXene nanosheets throughout the generated structures. However, increasing the MXene ratio from 3 to 5 wt% resulted in filler accumulation, evidenced by the clustering of titanium elements within the scaffold. The observed data is consistent with the results declared by Zhao *et al.*[22] At lower filler concentrations, MXene particles exhibit enhanced dispersion within the polymer matrix. The increased distance between nanosheets minimizes the potential for strong, attractive forces to cause aggregation, promoting a more uniform filler distribution in the films. In contrast, as the concentration of MXene rises, the likelihood of particle-to-particle interactions escalates significantly. The resultant strong interactions between MXene nanosheets become predominant, leading to considerable agglomeration and irregular MXene distribution within the polymer matrix.

The FTIR spectra of the blank GG and loaded GG with 1, 3, and 5 wt% MXene nanosheets are presented in Fig. 3a. Regarding the Pure GG structure, a significant broadband was observed at 3427 cm^{-1}, which could be linked to the –OH group vibration, providing the basic polysaccharide structure. The appeared peak could also be related to the stretching vibration of intermolecular hydrogen bonding. The peaks displayed at 2923 and 2852 cm^{-1} could be assigned to the $-CH_3$ and $-CH_2$ stretching vibrations of gellan gum. Moreover, the bands in the range of 1741–1637 and 1463 cm^{-1} were possibly

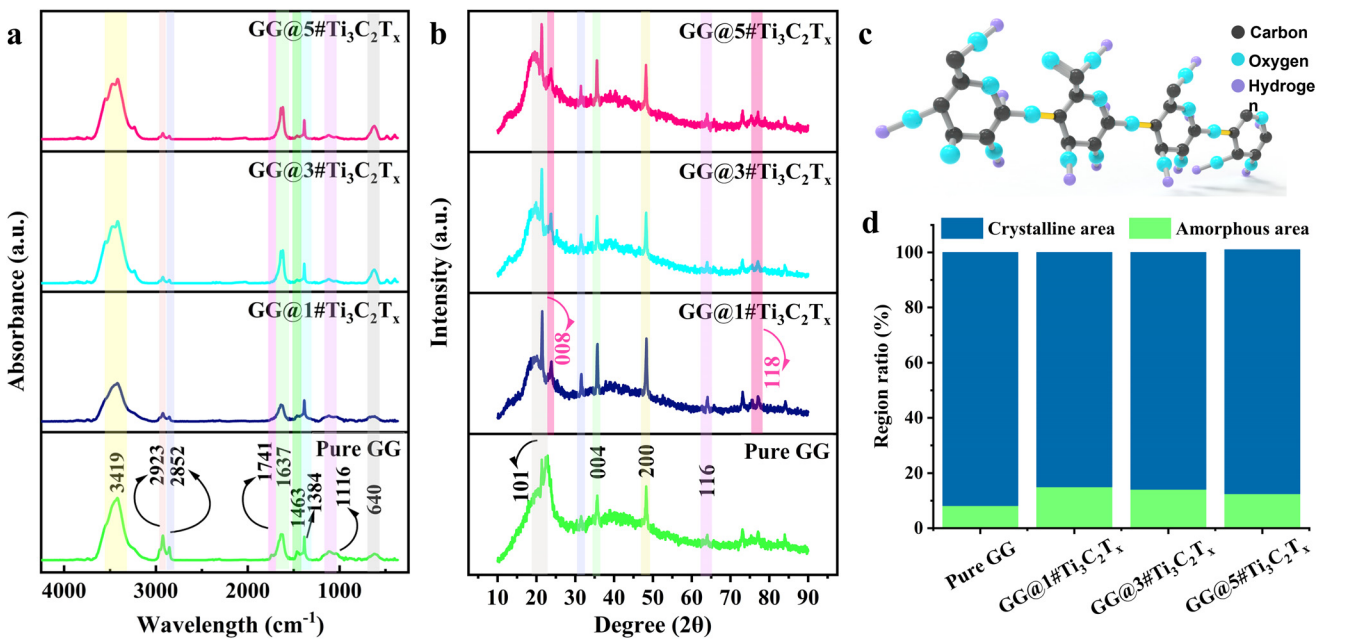

Fig. 3 Physiochemical features; (a) FTIR spectra and (b) XRD patterns of Pure GG, GG@1#$Ti_3C_2T_x$, GG@3#$Ti_3C_2T_x$, and GG@5#$Ti_3C_2T_x$ tissues, (c) chemical formula of gellan gum polymer used as polymer matrix, and (d) crystalline and amorphous regions in the generated scaffolds.

due to C=O stretching and –CH bending of the employed polymer matrix. The ethereal and hydroxylic C–O stretching vibrations were displayed at 1384 and 1116 cm^{-1}, respectively. Through embedding various ratios of the MXene filler into the GG-based structure, a shift was observed in the –OH group vibration from 3419 to 3415 cm^{-1}. In addition, a slight change was observed in the $–CH_2$ stretching vibrations *via* shifting from 2852 to 2850 cm^{-1}. The band at 1116 cm^{-1} was also transformed to 1120 (GG@1#$Ti_3C_2T_x$), 1126 (GG@3#$Ti_3C_2T_x$), and 1128 cm^{-1} (GG@5#$Ti_3C_2T_x$). The detected substitutions suggest a potential interaction between the gellan gum polymer chains and the embedded MXene nanosheets, thereby approving the successful dispersion of the MXene nano galleries in the gellan gum body. Based on their chemical compositions and the literature, the interactions might occur through electrostatic forces and hydrogen bonding. The surface terminal groups in the MXene nanogalleries likely interact electrostatically with the charged functional groups of gellan gum, which helps disperse and stabilize $Ti_3C_2T_x$ in the gellan gum matrix. Additionally, the MXene functional groups are able to interact with gellan gum hydroxyl groups through hydrogen bonds potentially, leading to improved adhesion and stability within the composite structure.[23]

XRD analysis was used to evaluate the crystal structure of Pure GG and MXene-loaded GG (Fig. 3b). The broad diffraction peaks that appeared in the X-ray diffractogram represented the semi-crystalline nature of the gellan gum matrix. The sharp peaks at 2θ degrees of 22.87, 35.67, 48.27, and 64.02° belonged to the 101, 004, 200, and 116 crystal planes in the gellan gum polymer.[24] Introducing the MXene nanosheets caused a slight change in the diffraction angles. The 101 crystal plane appeared at 21.47 (GG@1#$Ti_3C_2T_x$), 21.37 (GG@3#$Ti_3C_2T_x$), and 21.32° (GG@5#$Ti_3C_2T_x$). Additionally, the peak at 23.62° was shifted to 23.87° through loading various ratios of the MXene layered nanomaterial. The crystal 004 plane was transformed from 35.67° to 35.64, 25.62, and 35.57° *via* loading 1, 3, and 5 wt% MXene. Also, the diffraction peaks of 200 and 116 planes were observed at 48.32, 48.27, and 48.22°, alongside 64.01, 63.97, and 63.92° in GG@1#$Ti_3C_2T_x$, GG@3#$Ti_3C_2T_x$, and GG@5#$Ti_3C_2T_x$, respectively. Besides, a new peak appeared at 31.50 and 77° in the films filled with MXene nanosheets, corresponding to 008 and 118 crystal planes in $Ti_3C_2T_x$. The observed shifts in the angle of diffraction peaks might be a direct result of interactions between gellan gum and MXene nanosheets. By embedding the crystalline nature of MXene into the semicrystalline gellan gum network, the MXene nanosheets could be effectively dispersed within the polymer matrix, significantly reducing the probability of filler aggregation. Furthermore, the hydrophilic nature of gellan gum plays a crucial role in maintaining water uptake and swelling, consequently influencing the spacing behavior. Additionally, the MXene nanoflakes are unequivocally encapsulated within the gellan gum, as the polymer chains tightly wrap around or interpenetrate the MXene surfaces, thereby boosting mechanical and thermal stability. Therefore, these possible interactions undeniably lead to the formation of a mechanically robust, thermally stable, and potentially conductive composition.[25]

Chemical formula of the gellan gum employed as the polymer matrix of the developed structures is shown in Fig. 3c. The crystalline zone and amorphous area of the prepared composites were estimated as presented in detail Fig. 3d. Based on the obtained data, the amorphous area was inclined from 8.18 to 15% *via* loading 1 wt% $Ti_3C_2T_x$. The observed trend in the crystallinity could be linked to the disruption of well-packed gellan gum chains, which hindered the crystallization procedure by the presence of layered MXene in the structure. Meanwhile, further increments in the MXene concentration led to a reduction in the amorphous zones to 12.5%. The observed enhancement in the crystalline region could be assigned to the nucleating agent behavior of the MXene nanosheets, integrating the crystallization by providing heterogeneous nucleation sites. This results in the creation of more organized regions during solvent evaporation, which is in line with the work carried out by Banitaba *et al.*[26]

3.3 Analysis of the thermal stability in the developed architectures

Thermal stability is one of the favorable characteristics of the MXene nanoarchitectures. Accordingly, introducing the MXene nanosheets into a polymeric structure may influence the thermal stability of the generated composition. To explore the impact of $Ti_3C_2T_x$ on the thermal stability of gellan gum-based films, TGA and DSC analysis were conducted (see Fig. 4a–d). As is illustrated in the obtained TGA thermograms, the onset temperature decomposition (T_d) was inclined from 172 to 184 °C by loading 3 wt% MXene into the polymeric network. Meanwhile, exceeding this optimized concentration caused a reduction in the T_d value to 160 °C. The observed increase in T_d could be credited to the MXene fillers acting as a thermal stabilizer in the gellan gum-based structure. The presence of $Ti_3C_2T_x$ in the composition can potentially strengthen the polymer matrix, enhance heat dissipation, and improve thermal stability. Additionally, the MXene nanogalleries are capable of absorbing heat, resulting in an improved T_d. However, it is vital to note that overloading the filler beyond the optimal range may create more interfaces where degradation can occur, potentially compromising the even dispersion of MXene in the polymeric structure. This could lead to a slight decrease in T_d due to the formation of weak points in the matrix, accelerating thermal degradation.[27] After burning the polymer matrixes, the weights of 19, 22, 27, and 28% remained in the Pure GG, GG@1#$Ti_3C_2T_x$, GG@3#$Ti_3C_2T_x$, and GG@5#$Ti_3C_2T_x$, respectively. This could be attributed to the remaining mass of the MXene element in the compositions, approving the successful incorporation of $Ti_3C_2T_x$ in the gellan gum-based structures.

In virtue of the DSC profile, the broad endothermic peaks appearing at around 110 to 120 °C could be related to the evaporation of water from the specimens. Also, the observable exothermic peaks at 299, 358, 411, and 311 °C might be attributed to the thermal decomposition of the polysaccharide struc-

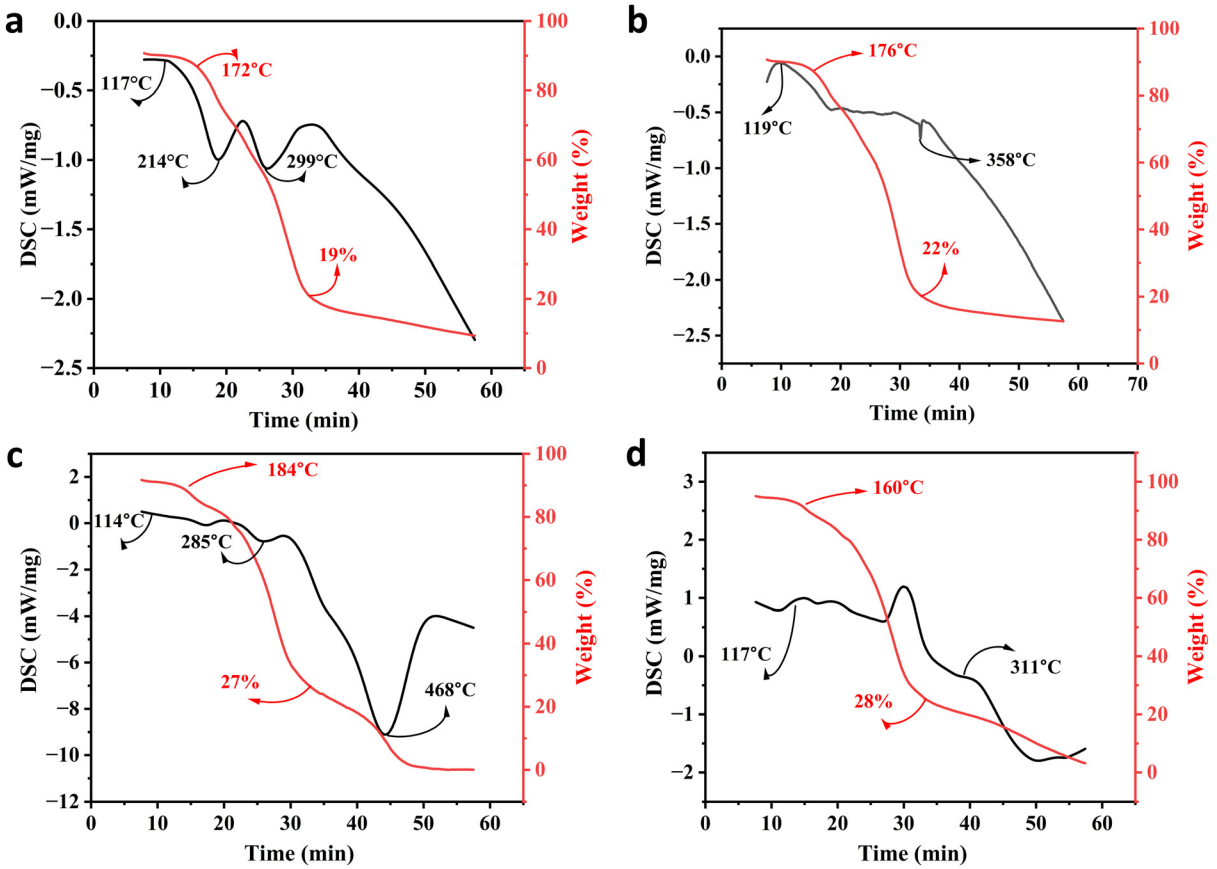

Fig. 4 Thermal stability of the generated architectures; TGA and DSC analysis of the (a) Pure GG, (b) GG@1#$Ti_3C_2T_x$, (c) GG@3#$Ti_3C_2T_x$, and (d) GG@5#$Ti_3C_2T_x$ scaffolds.

tures. Therefore, the structural decomposition was mainly a result of the decay in the polymeric component alongside the water volatilization. Hence, in line with the devoted attempts in the literature, there was no evidence regarding the degradation of MXene in the developed networks.[22]

3.4 Hydrophilicity of the membranes

The contact angle of the generated compositions was measured to assess how the MXene component affects the membranes' hydrophilicity (refer to Fig. 5a–e). According to the data, the Pure GG specimen revealed a contact angle of 36.8°. However, incorporating MXene nanocomposites into the scaffolds resulted in a decrease in the contact angle to an approximate value of 30°, possibly due to its layered structure terminated with hydroxyl and other polar groups. Compared to GG@1#$Ti_3C_2T_x$ (27.5°) and GG@3#$Ti_3C_2T_x$ (30.01°), the GG@5#$Ti_3C_2T_x$ scaffold unveiled a higher contact angle of 31.4°. This might correspond to the formation of a compact membrane with reduced surface roughness due to the MXene microsphere adhesion, as indicated from the data obtained from FESEM and AFM images. Surface roughness is an important factor influencing hydrophilic behavior and contact angle.[28,29] It is notable that the tissue loaded with 1 wt% $Ti_3C_2T_x$ possessed a slighter contact angle than the one integrated with 3 wt% MXene, indicating higher hydrophilicity. This result might be attributed to the advanced surface roughness of the GG@1#$Ti_3C_2T_x$ structure and the disparities in the sizes of MXene microspheres.

The spreading coefficient of the designed compositions is depicted in Fig. 5f. This parameter is commonly used to measure how well a liquid wet a solid surface. When the spreading coefficient is negative, it means that the liquid does not spread out on the surface and instead forms droplets. This occurs because the energy at the liquid–solid boundary is higher than the combined energies at the liquid–vapor and solid–vapor boundaries.[30] As is apparent, the spreading coefficient approached zero over time, indicating that the surface became increasingly wettable by the liquid as time progressed. Fig. 5g also exhibits the work of adhesion (Wadh), referring to the energy required to separate two adherent surfaces. This positive quantity indicates the strength of the bond between the surfaces, with a higher value of Wadh reflecting a stronger bond. The results showed the highest adhesion performance in the specimen containing 1 wt% $Ti_3C_2T_x$. Although no substantial difference was observed between the MXene-loaded scaffolds, all mediated films displayed statistically significant promoted Wadh than the blank gellan gum network. as evidenced by the three average contact angles, spreading coefficient, and work of

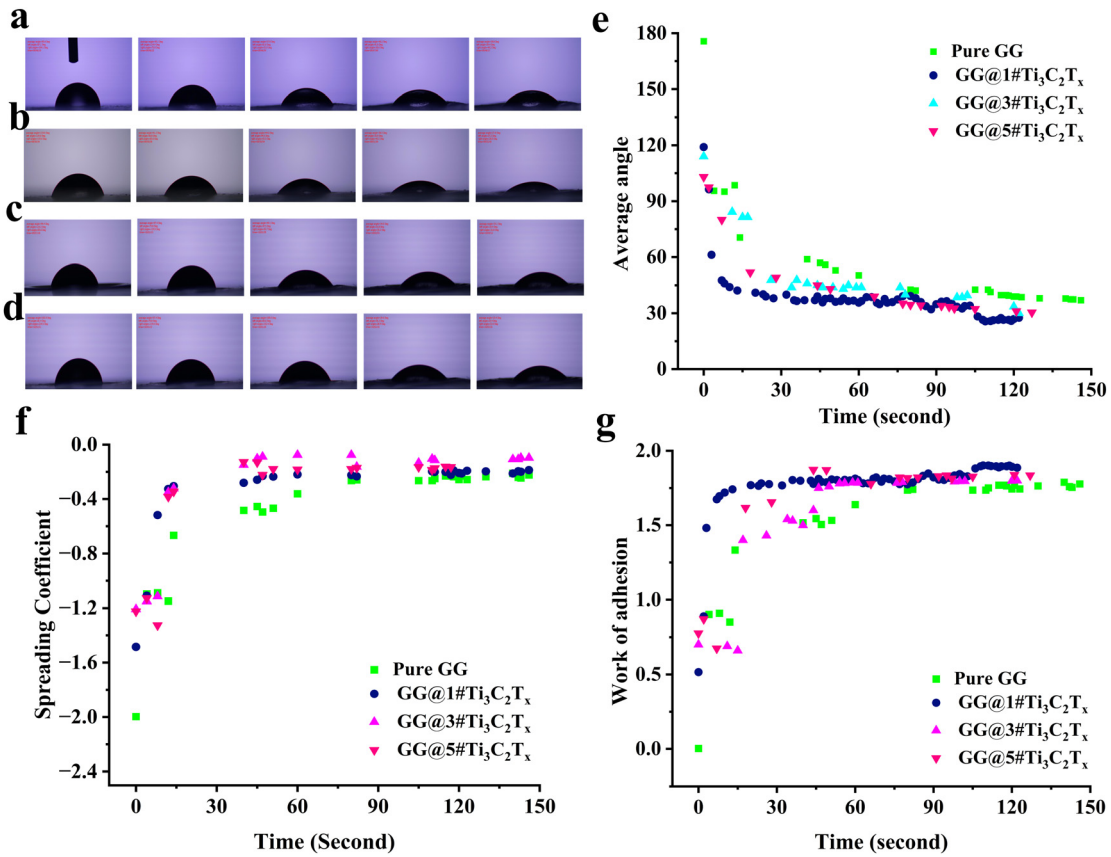

Fig. 5 Hydrophilicity features; contact angle images of (a) Pure GG, (b) GG@1#$Ti_3C_2T_x$, (c) GG@3#$Ti_3C_2T_x$, and (d) GG@5#$Ti_3C_2T_x$ composites, (e) maturation trends of sample's average angle, and the time-dependent behavior of (f) spreading coefficient and (g) work of adhesion.

adhesion factors, the interfacial adhesion of MXene was influenced by its surface energy, which aligns with the findings reported by Zukiene *et al.*[31] In essence, the presence of MXene served to augment the hydrophilicity of the surface, following the conclusions drawn from the research conducted by Rakhmanov *et al.*,[32] Machata *et al.*,[33] and Zhou *et al.*[34]

3.5 Mechanical and swelling behavior of the designed tissues

Incorporating fillers into polymeric films significantly influences their mechanical properties. Research indicates that adding a low to moderate ratio of fillers enhances tensile strength while surpassing an optimal concentration can result in reduced mechanical performance due to filler agglomeration and ineffective stress transfer. Understanding these dynamics is essential for developing optimized filler-loaded compositions.[35] The preparation of samples for estimating their mechanical behavior is schematically presented in Fig. 6a. Fig. 6b and c also present the data attained through analyzing the mechanical features. Consequently, loading 1 wt% MXene into the gellan gum-based structure significantly heightened the mechanical features, improving the stress by 46.8% and increasing Young's modulus from 11.28 to 13.43 MPa. The observed boosting in the mechanical properties could be due to introducing additional bonding sites *via* loading MXene layered nanomaterial into the structure, promoting the polymeric structure's overall integrity and cohesion.[36] However, further increments in the loading ratio caused a decline in the stress by 18% (GG@3#$Ti_3C_2T_x$) and 19% (GG@5#$Ti_3C_2T_x$), along with a decrease in Young's modulus to 13.01 MPa (GG@3#$Ti_3C_2T_x$) and 12.46 MPa (GG@5#$Ti_3C_2T_x$). The statistical analysis demonstrated a significant increase in stress with the addition of 1 wt% MXene. Moreover, the marked decline in stress when raising the MXene ratio from 1 to 3 wt% was compellingly significant. Importantly, our findings indicated no notable difference in stress values between the GG@3#$Ti_3C_2T_x$ and GG@5#$Ti_3C_2T_x$ samples, emphasizing the consistency of results at these higher concentrations. Also, no significant differences were observed between the strain values of the MXene-loaded scaffolds. The attained results could be assigned to the filler accumulation, which is accounted for as a defect in the developed polymeric networks. In accordance with the literature, the created agglomerations lead to insufficient load transfer, alongside the formation of weak points in the polymer matrixes. Moreover, high filler loading may hinder the ability of polymer chains to interact effectively, decreasing the tensile strength.[36] These data align with the EDS mapping provided for the designed specimens, showing the agglomeration of

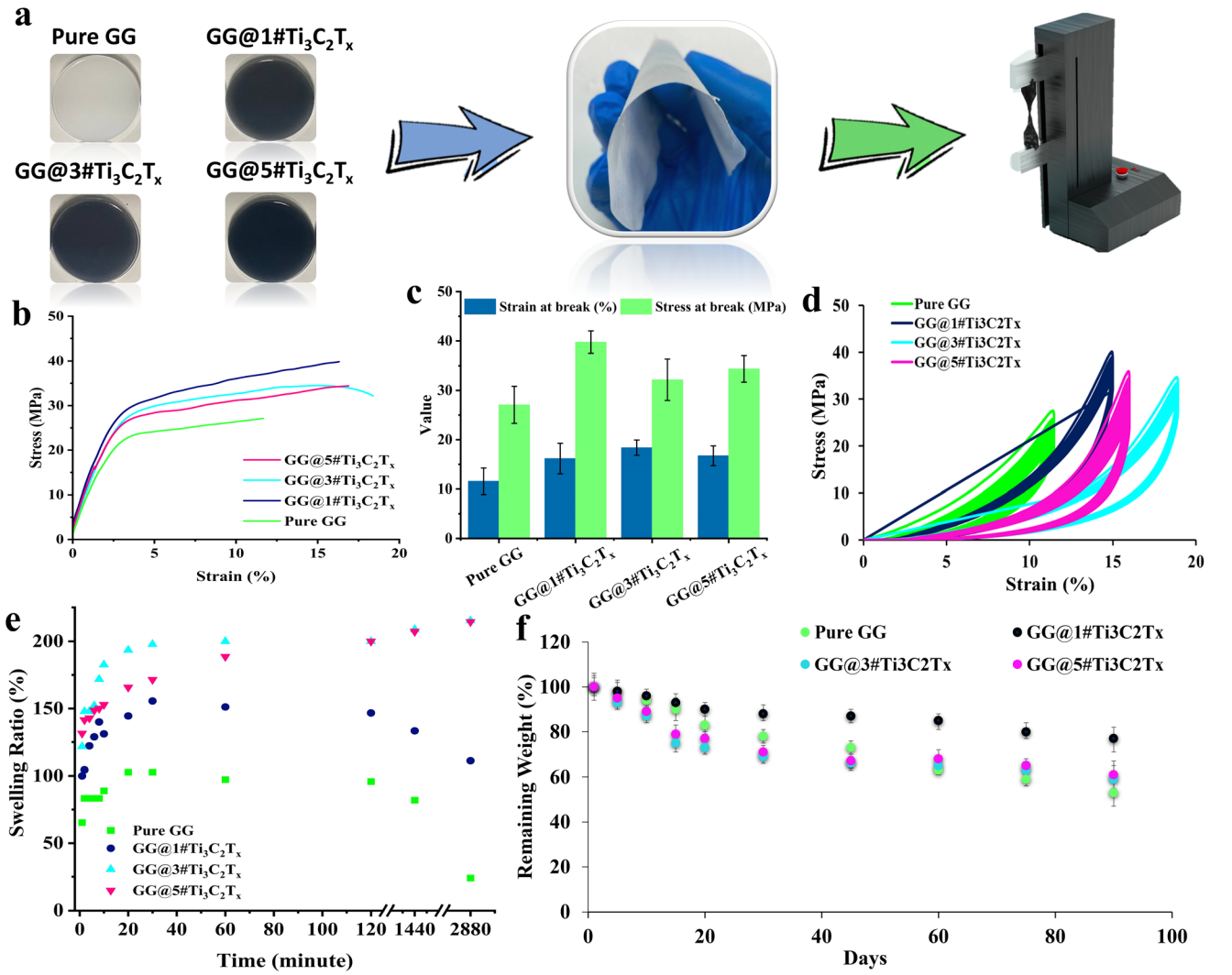

Fig. 6 Mechanical feature, swelling ratio, and degradation rate of Pure GG and loaded samples with 1, 3, and 5 wt% MXene; (a) illustration of the sample preparation for mechanical analysis, (b and c) mechanical strength, (d) cyclic stress–strain curves, (e) swelling ratio in 48 h, and (f) degradation rate in PBS during 90 days.

titanium in high filler loading ratios. Therefore, to achieve the best mechanical performance, incorporating 1 wt% MXene nanosheets into the gellan gum-based composition is essential. It is important to note that increasing the MXene content beyond this level could adversely impact the material's mechanical properties.

Cyclic stress–strain curves of the designed structures are shown in Fig. 6d. Commonly, the hysteresis indicates that the unloading curve approaches the *X*-axis more closely than the loading curve. The area encompassed within the hysteresis loop represents the energy loss, primarily manifested as heat, due to internal friction.[37] From the figure it can be seen that, all samples displayed a fully closed hysteresis loop and exhibited nearly identical areas of hysteresis or energy loss. Concerning the role of MXene, the observed trend in the rupture test aligns with the stress and strain characteristics of the samples. The MXene-loaded samples demonstrated the lowest levels of hysteresis or energy loss compared to the pure sample. This observation might be attributed to the fact that the molecular chains in the MXene-containing samples are subjected to a reduced degree of loading.[37] Consequently, the presence of MXene could lead to a more stable performance under long-term load-bearing conditions, which could be approved by coinciding the curves in various cycles.

The scaffold weight trend in the designed films was also assessed for 48 h using DI. Based on the obtained results exhibited in Fig. 6e, swelling occurred in all samples in the first 40 minutes. Through the addition of MXene nanosheets up to 3 wt%, the swelling behavior was amplified from 102 to 197%. However, further increment in the MXene ratio to 5 wt% caused a decay in the swelling ratio to 171%. The observed trend could be attributed to the complex effect of MXene on the swelling ratio of the polymers. In low concentrations, the hydrophilic nature of MXene could result in the

attraction of water molecules, contributing to augmented swelling of the polymer matrix. Additionally, the layered architecture of MXene might allow for the intercalation of solvent molecules between the MXene layers, leading to a rise in the interlayer spacing and a sophisticated swelling ratio. Meanwhile, further increment in the concentration could cause the barrier function of MXene layers against water molecules, hindering the penetration of water molecules between the polymer chains.[38] It is worth noting that Pure GG and GG@1#$Ti_3C_2T_x$ experienced degradation after this time point, while GG@3#$Ti_3C_2T_x$ and GG@5#$Ti_3C_2T_x$ remained stable and continued to swell for 48 h. The observed stability in the samples integrated with 3 and 5 wt% MXene could be related to the difficulty of water molecules' penetration into the polymer matrix and their direct impact on slowing down the degradation.

The degradation rate of the samples was also examined, as shown in Fig. 6f. The provided data could demonstrate the effect of the MXene ratio on the degradation rate of the fabricated structure in PBS solution over a period of 90 days. Specifically, the addition of 1 wt% MXene improved the mass ratio, likely due to the electrostatic interactions between the surface terminal groups of MXene and the functional groups of the gellan gum. Additionally, hydrogen bonding between the functional groups of MXene and the hydroxyl groups of gellan gum was confirmed from the FTIR spectrum. In fact, the strong interaction between the loaded filler and the gellan gum polymer chains enhanced stability in the PBS environment. An increase in the MXene ratio, however, resulted in decreased stability and a higher degradation rate. This effect is likely due to the agglomeration of the fillers, which hinders appropriate interactions between the filler particles and the gellan gum polymer chains.[27] The results obtained are consistent with the EDS spectra, as well as the analyzed mechanical properties and swelling ratios of the samples.

3.6 Biological features of the designed structures

The developed membranes underwent assessment for cytotoxicity and osteogenic cell adhesion. As depicted in Fig. 7a and b, the cytotoxicity assay revealed close to 100% cell viability in all samples. This observation proved that the presence of MXene not only exhibits non-toxic properties but also supports cell survival on the scaffold's surface. The remarkable compatibility between $Ti_3C_2T_x$ nanosheets and MG63 cells yielded promising results. The findings highlighted the thriving state of the majority of MG63 cells in both the control group and tissues embedded with 1, 3, and 5 wt% MXene nanosheets. These exciting results underscored the potential of MXene nanosheets in promoting cell health and function, which agrees well with previously reported data, declaring that the robust binding capacity of MXene nanoflakes to MG63 cells is attributed to the electrostatic interactions formed between the negative charges of MXene and the positive charges of cell proteins.[13]

In the images labeled Fig. 7c and d, the account and adhesion of MG63 cells on various compositions, including Pure GG, GG@1#$Ti_3C_2T_x$, GG@3#$Ti_3C_2T_x$, and GG@5#$Ti_3C_2T_x$ after 24 h is depicted. According to the results, the successful adhesion of cells in all GG-based tissues was perceived. The attained cell adhesion might be attributed to the presence of both the bio-based polymer and the MXene element in the compositions, augmenting the adhesion, roughness, and hydrophilicity in the structures.[39,40] The introduction of 1 wt% MXene resulted in a higher cell count and appropriate cell adhesion, likely due to the increased hydrophilicity and surface roughness, as previously confirmed from the contact angle and AFM results. Meanwhile, higher MXene content led to a significant reduction in the cell count and cell adhesion, which could be caused by the different topographies of the developed structures, as approved by AFM images. In the case of incorporating 3 and 5 wt% MXene, the filler grains might tend to get close to each other, making a decreased or unstable roughness in the surface. Therefore, it appears that the hindrance of appropriate roughness in the GG@5#$Ti_3C_2T_x$ could be another reason for the poor cell adhesion observed.[41]

3.7 Bactericidal properties of the architectures

This study investigated the antibacterial activity of the prepared membranes against *S. aureus* and *E. coli*, as depicted in Fig. 7e. The GG membrane exhibited an impressive inhibition zone of 4.3 ± 0.4 mm against *S. aureus* bacteria, highlighting the potential of the developed polymeric network to combat harmful bacteria. Additionally, adding 1, 3, and 5 wt% MXene into the gellan gum-based structure resulted in an upsurge in the inhibition halo to 4.8 ± 0.2, 5.1 ± 0.6, and 5.2 ± 0.4 mm, as evidenced in Fig. 7e. Similarly, the zone diameter against *E. coli* enlarged from 4.9 ± 0.3 mm to 5.0 ± 0.1, 5.4 ± 0.4, and 5.6 ± 0.2 mm with the intensification in the MXene ratio from 1 to 5 wt%. These findings confirmed the dual antibacterial behavior of the fabricated membranes. Based on the compelling data gleaned from histograms, it is fascinating to note that the larger diameter breakpoints observed against Gram-negative bacteria compared to Gram-positive bacteria can be attributed to the formidable defense provided by the thicker peptidoglycan cell walls of *S. aureus*. This superior protection against antibacterial effects underscores the remarkable resilience of *S. aureus* in the face of microbial challenges.[42] On the other hand, as a natural-based polymer, gellan gum has antibacterial properties, which was expected to be boosted through the incorporation of MXene nanoflakes.[8,43] As a result, the presence of MXene in the gellan gum-based membranes enhanced antibacterial behavior, supporting the direct impact of MXene nanosheets on the antibacterial efficiency. This outcome could be explained through the disruption of the outer cell walls of the bacteria *via* the sharp edges of $Ti_3C_2T_x$, leading to severe breakdown of cell membranes and cytoplasm leakage. Moreover, based on the literature, the hydrophilicity of MXene networks incapacitates the bacteria and increases their killing rates. The interaction between MXene groups and bacteria's lipopolysaccharide cords principals to H-bonding, reducing the bacteria's nutrition. Additionally, the diminutive MXene nanosheets have the capacity to infiltrate bacteria

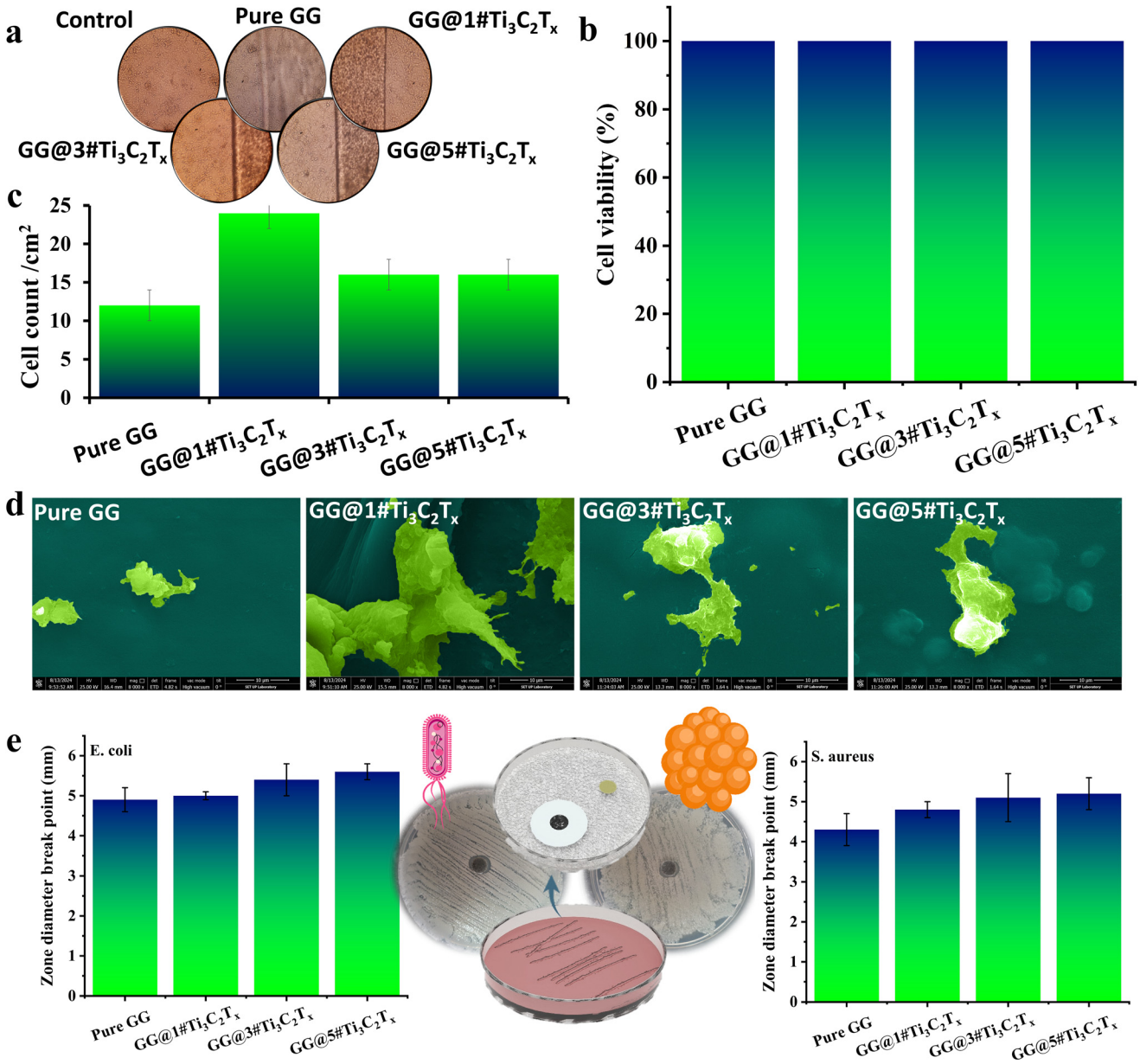

Fig. 7 Cell cytotoxicity, cell adhesion, and antibacterial properties; (a and b) cytotoxicity behavior and cell viability of the tissues, (c) cell count in various samples, (d) cell adhesion on the Pure GG, GG@1#$Ti_3C_2T_x$, GG@3#$Ti_3C_2T_x$, and GG@5#$Ti_3C_2T_x$ scaffolds, and (e) antibiogram examination of the developed architectures against *E. coli* and *S. aureus*.

through direct endocytosis or indirect penetration ways, causing disruption to the bacteria's DNA.[11] The delicate crystallite grains of $Ti_3C_2T_x$ nanosheets are postulated to facilitate closer interaction with the bacteria, subsequently yielding heightened antibacterial efficacy.[44] Furthermore, an escalation in the $Ti_3C_2T_x$ concentration might engender increased entrapment and aggregation of bacteria between the filler sheets, thereby augmenting antibacterial behavior.

Despite the efforts invested, the fabricated structure still exhibited the potential for improvement in its cellular and antibacterial properties. Consequently, the optimization process was initiated by integrating porosity into the film-based structure. Furthermore, to fortify the antibacterial properties, the incorporation of garlic extracts was employed as advocated in the literature.[15] Subsequently, the modified structure underwent rigorous structural evaluation in addition to cellular and antibacterial analyses.

3.8 Conjugated MXene-loaded film with garlic extract

Two strategies were employed to tackle the problems related to the optimized MXene-loaded film (GG@1#$Ti_3C_2T_x$). In the virtue of material components, garlic extract (1 and 3 ml) was conjugated with the material composition. Garlic extract, particularly its bioactive compound allicin, holds promising

potential in tissue engineering, offering a range of benefits that can promote cell growth, tissue regeneration, and overall scaffold performance.[45] Also, the freeze-drying procedure was utilized to develop highly porous architectures of GG@1#$Ti_3C_2T_x$@1#GA and GG@1#$Ti_3C_2T_x$@3#GA. Fig. 8a and b represent FESEM images of the freeze-dried samples containing various amounts of the garlic extract. Using the freeze-drying procedure, porous structures with interconnected fine pores were formed. However, an increase in the garlic extract amount from 1 to 3 ml tended to reduce the porosity by forming a denser structure.

Fig. 8c shows the attained FTIR spectra of the prepared tissues. Based on the literature, the garlic extract shows several characteristic peaks at about 3265, 2926, 1619, 1396, and 1036 cm^{-1} corresponding to hydroxyl (–OH), aromatic (–CH), carbonyl and carboxylic (C═O), carboxylic (–OH), and organo-sulfur (SO) functional groups, respectively. Compared to the FTIR spectrum of GG@1#$Ti_3C_2T_x$, some changes were observed, which could be attributed to the overlap of the characteristic peaks alongside interactions between the elements. Accordingly, a slight shift was observed in the –OH bond from 3415 to 3438 cm^{-1}. In addition, the –CH_2 and C═O stretching vibrations were shifted to 2854 and 1639 cm^{-1}, respectively. The C–O stretching peak also appeared at 1114 cm^{-1}. The observed changes could be related to the interaction between the components in the generated composites. According to the chemical structures of the garlic extract and gellan gum polymer, hydrogen bonding probably occurred between the sulfur atoms in the garlic extract and the hydroxyl groups of gellan gum. The hydrophobic tail of allicin in the garlic extract might also interact with the hydrophobic regions in the gellan gum structure.

The impact of garlic extract on the hydrophilicity of the MXene-loaded film was investigated, as shown in Fig. 8d–f. The impact of garlic extract on the hydrophilicity of polymeric membranes highly depends on its type and concentration.[45] According to the data gained, a low concentration of garlic extract led to an enhancement in the hydrophilicity, while further increments in the garlic ratio influenced the hydrophobic nature. This could be linked to the complex nature of the garlic, comprising both hydrophobic and hydrophilic zones. Based on its chemical structure, allicin provides a hydrophobic section in the garlic extract (see Fig. 8g). Also, garlic contains sulfur compounds, some hydrophobic and some hydrophilic. The garlic structure having sugar, amino acids, and vitamins has a hydrophilic nature. The cell attachment behavior of the samples is also depicted in Fig. 8h and i. Compared with the GG@1#$Ti_3C_2T_x$ film, the GG@1#$Ti_3C_2T_x$@1#GA film exhibited better cell attachment, which probably could be attributed to the formation of tiny pores in the structure, along with the presence of garlic extract. The literature suggests that an optimized freeze-drying procedure can create fine, interconnected pores in the polymeric network. This interconnectivity is crucial for cell migration, nutrient diffusion, and waste removal within the scaffold. If the scaffold lacks sufficient interconnectivity, cells may become trapped in isolated regions, which could impede tissue regeneration. Therefore, porous structures enable cell

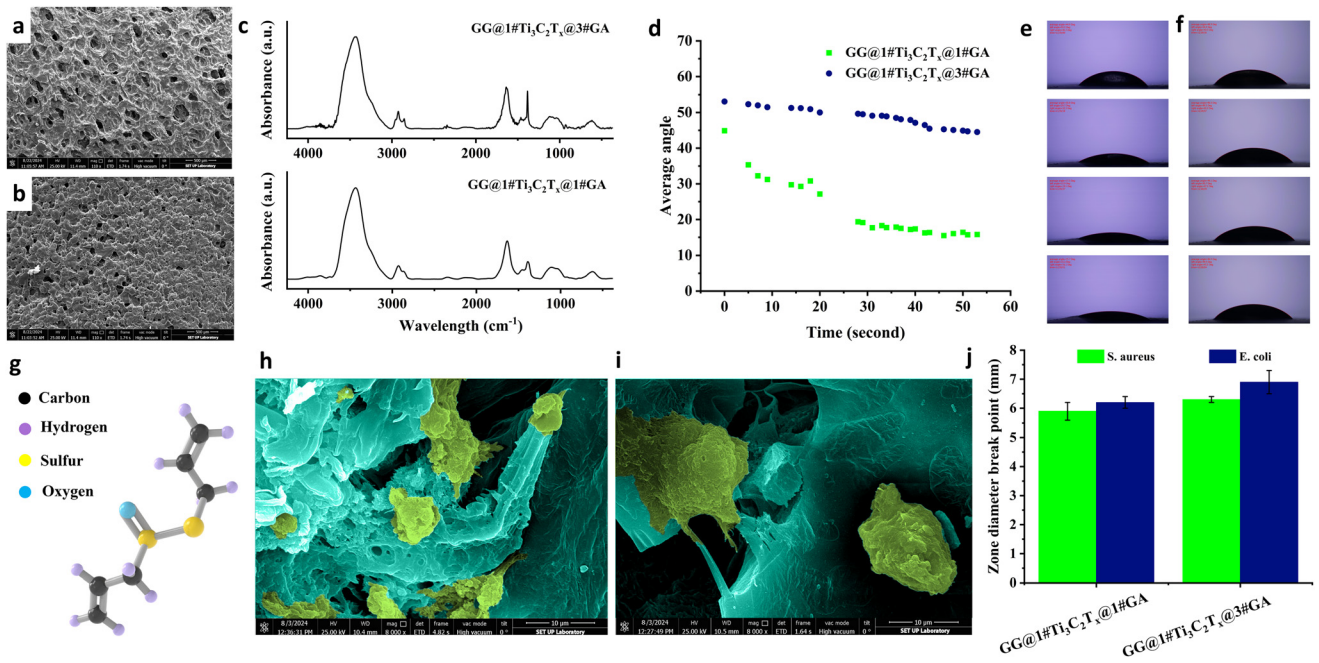

Fig. 8 Characteristics of the freeze-dried GG@1#$Ti_3C_2T_x$ polymeric network loaded with 1 and 3 ml garlic extract; FESEM images of (a) GG@1#$Ti_3C_2T_x$@1#GA and (b) GG@1#$Ti_3C_2T_x$@3#GA, (c) FTIR spectra, (d) average contact angle *vs.* time, (e and f) contact angle illustrations of the loaded sample with 1 and 3 ml garlic extract, (g) chemical formula of allicin, cell attachment behavior in (h) GG@1#$Ti_3C_2T_x$@1#GA and (i) GG@1#$Ti_3C_2T_x$@3#GA, and (j) antibacterial activity against *S. aerous* and *E. coli*.

attachment by providing a superior surface area to interact with the material and more potential sites for cell adhesion, as well as facilitating the diffusion of nutrients, oxygen, and growth factors *via* pore spaces.[46] Several studies have also highlighted the remarkable potential of garlic extract, especially its allicin component, to enhance cell adhesion to polymer surfaces significantly. This enhancement occurs by modifying polymer surfaces through adding or altering functional groups, improving adhesion, and fostering anti-inflammatory properties. Inflammation significantly hinders bone cell adhesion and integration within a scaffold. By incorporating garlic extract into the process, inflammation can be effectively reduced, enhancing the success of bone healing and integration. Moreover, the antioxidant compounds found in garlic extract play a crucial role in shielding cells from oxidative damage, thereby promoting their growth. Additionally, garlic extracts are known to modulate the immune system, providing an indirect yet impactful boost to cell growth and proliferation.[47] As is apparent in the attained FESEM images, the designed tissue loaded with 3 ml garlic extract seems to have inferior cell attachment than the one incorporated with 1 ml garlic element, which might be due to the occurred depletion in its porosity rate.

Fig. 8j displays the activity of the integrated tissues with garlic extract against Gram-positive and Gram-negative bacteria. According to the results, the inhibition ring was significantly increased by incorporating 1 ml garlic extract to 5.9 ± 0.3 and 6.2 ± 0.2 mm against *S. aureus* and *E. coli*, respectively. Further increment in the garlic extract loading also led to an enhancement in the inhibition ring up to 6.3 ± 0.1 (*S. aureus*) and 6.9 ± 0.4 mm (*E. coli*), which could be directly related to the existence of more allicin elements in the structure acting as antimicrobial agents. The observed difference between the antibacterial results against two considered Gram-positive and Gram-negative bacteria could be assigned to the designed material compositions. *S. aureus* and *E. coli* represent two distinct categories of bacteria with critical implications for treatment. As discussed above, *S. aureus* is classified as Gram-positive, while *E. coli* is Gram-negative. This fundamental variation in their cell wall structures significantly affects their responsiveness to antibiotics. The thick peptidoglycan layer in Gram-positive bacteria makes them particularly vulnerable to antibiotics targeting this structure. In contrast, an outer membrane in Gram-negative bacteria, composed of lipopolysaccharides, presents a formidable barrier against many substances. This barrier means that specific antibiotics, particularly those that interfere with peptidoglycan synthesis, excel in combatting Gram-positive infections. Conversely, antibiotics that disrupt protein synthesis are more effective against *E. coli* and similar bacteria. It is essential to consider not only the choice of antibiotic but also the formulation and concentration of active ingredients, as these factors can greatly influence the treatment success.[48] Based on the literature, allicin could show more activity against *S. aureus* compared with *E. coli*. This could be attributed to the ability of allicin to pass the lipid section of the *S. aureus* organism membrane, influencing the RNA mechanism, membrane lysis, and bactericidal impact.[49] However, in the developed architectures in the present study, more antibacterial behavior was observed against *E. coli*, which could be due to the presence of both allicin and MXene in the designed architectures, leading to a synergetic impact on combating *S. aureus* and *E. coli*. It is important to note that while using 3 ml of garlic extract yields improved antibacterial results, the optimal amount is actually 1 ml. This smaller dosage minimizes side effects, such as blocking pores, and provides more ideal conditions for cell growth and attachment.

4. Conclusion

In summary, the GG/MXene/GA ternary system was designed to replicate the bone structure. In this regard, a $Ti_3C_2T_x$ MXene nanomaterial was successfully synthesized and integrated into GG-based scaffolds with various 1, 3, and 5 wt% content ratios. The results exhibited that 1 wt% $Ti_3C_2T_x$ could be homogeneously hybridized in the GG network, revealing a reduced crystallinity of 15%, a superior hydrophilicity of about 27.5°, and a significantly enhanced Young's modulus up to 13.43 MPa. In addition, the tissue loaded with $Ti_3C_2T_x$ MXene nanosheets showed no signs of cytotoxicity and fostered stronger adhesion of human osteoblast cells to the structure. What's more, these scaffolds exhibited heightened antimicrobial capabilities against both *S. aureus* and *E. coli* bacteria, showcasing their remarkable multifunctional nature. Further enhancement in the biological performance of the scaffold characteristics could also be approached through embedding GA into the freeze-dried MXene-loaded GG architecture. Based on the results, both cell adhesion and antibacterial activities were promoted in the GA-medicated highly porous polymeric structure. It should be underlined that a balance is required between mechanical properties, bioactivity behavior, and antibacterial performance, generating versatile bone tissue that effectively combats implant-associated infections. In conclusion, the specific ratio of MXene and the incorporation of GA could result in exceptional scaffolding materials for bone tissue regeneration. Therefore, this research is expected to serve as a catalyst for further exploration of the application of MXenes in tissue engineering and regeneration of the body's primary anatomical structures by lighting the spark to take advantage of MXene triplex systems.

Author contributions

Lin Zhou: conceptualization, methodology, and software. Zhuo Zhao: data curation, methodology, and software. Xin Han: writing – original draft preparation, visualization, and supervision. Guang Chen: conceptualization, visualization, and supervision. Seyedeh Nooshin Banitaba: conceptualization and writing – reviewing and editing. Sanaz Khademolqorani: conceptualization and writing – reviewing and editing.

Data availability

The authors confirm that the data supporting the findings of this study are available within the article or its ESI.†

Conflicts of interest

The authors have no conflicts of interest to declare.

References

1 C. Willers, N. Norton, N. C. Harvey, T. Jacobson, H. Johansson, M. Lorentzon, *et al.*, Osteoporosis in Europe: a compendium of country-specific reports, *Arch. Osteoporos.*, 2022, **17**(1), 23.
2 S. Khademolqorani, H. Tavanai, I. S. Chronakis, A. Boisen and F. Ajalloueian, The determinant role of fabrication technique in final characteristics of scaffolds for tissue engineering applications: A focus on silk fibroin-based scaffolds, *Mater. Sci. Eng., C*, 2021, **122**, 111867.
3 P. Pan, Y. Hu, C. Wang, Q. Liu, L. Hu, H. Yu, *et al.*, Abalone shells bioenhanced carboxymethyl chitosan/collagen/PLGA bionic hybrid scaffolds achieving biomineralization and osteogenesis for bone regeneration, *Int. J. Biol. Macromol.*, 2024, **279**, 135018.
4 S.-J. Chang, S.-M. Kuo, W.-T. Liu, C.-C. G. Niu, M.-W. Lee and C.-S. Wu, Gellan gum films for effective guided bone regeneration, *J. Med. Biol. Eng.*, 2010, **30**(2), 99–103.
5 K. Loukelis, D. Papadogianni, J. E. Kruse and M. Chatzinikolaidou, The effects of gellan gum concentration on electrospinning and degradation of flexible, crosslinker-free scaffolds for bone tissue engineering, *Carbohydr. Polym. Technol. Appl.*, 2024, **7**, 100454.
6 U. D'Amora, A. Ronca, S. Scialla, A. Soriente, P. Manini, J. W. Phua, *et al.*, Bioactive composite methacrylated gellan gum for 3D-printed bone tissue-engineered scaffolds, *Nanomaterials*, 2023, **13**(4), 772.
7 S. Khademolqorani, S. N. Banitaba, S. Azizi and M. Kouhi, Gellan gum–based nanocomposite hydrogels, in *Application of Gellan Gum as a Biomedical Polymer*, Elsevier, 2024, pp. 171–197.
8 X. Li, S. Wang, M. Zheng, Z. Ma, Y. Chen, L. Deng, *et al.*, Synergistic integration of MXene nanostructures into electrospun fibers for advanced biomedical engineering applications, *Nanoscale Horiz.*, 2024, **9**(10), 1703–1724.
9 Y. Zhang, J. Li, V. H. M. Mouser, N. Roumans, L. Moroni and P. Habibovic, Biomimetic Mechanically Strong One-Dimensional Hydroxyapatite/Poly(d,l-lactide) Composite Inducing Formation of Anisotropic Collagen Matrix, *ACS Nano*, 2021, **15**(11), 17480–17498.
10 K. Rasool, M. Helal, A. Ali, C. E. Ren, Y. Gogotsi and K. A. Mahmoud, Antibacterial Activity of Ti3C2Tx MXene, *ACS Nano*, 2016, **10**(3), 3674–3684.
11 H. Li, M. Mu, B. Chen, L. Zhou, B. Han and G. Guo, MXene-based nanomaterials for antibacterial and wound healing, *Mater. Res. Lett.*, 2024, **12**(2), 67–87.
12 J.-H. Jang and E.-J. Lee, Influence of MXene particles with a stacked-lamellar structure on osteogenic differentiation of human mesenchymal stem cells, *Materials*, 2021, **14**(16), 4453.
13 J. Zhao, T. Wang, Y. Zhu, H. Qin, J. Qian, Q. Wang, *et al.*, Enhanced osteogenic and ROS-scavenging MXene nanosheets incorporated gelatin-based nanocomposite hydrogels for critical-sized calvarial defect repair, *Int. J. Biol. Macromol.*, 2024, **269**, 131914.
14 H. F. Liang, Y. P. Zou, A. N. Hu, B. Wang, J. Li, L. Huang, *et al.*, Biomimetic Structural Protein Based Magnetic Responsive Scaffold for Enhancing Bone Regeneration by Physical Stimulation on Intracellular Calcium Homeostasis, *Adv. Healthcare Mater.*, 2023, **12**(32), 2301724.
15 S. Bose, D. Banerjee and A. A. Vu, Ginger and garlic extracts enhance osteogenesis in 3D printed calcium phosphate bone scaffolds with bimodal pore distribution, *ACS Appl. Mater. Interfaces*, 2022, **14**(11), 12964–12975.
16 S. Bose, S. F. Robertson and A. A. Vu, Garlic extract enhances bioceramic bone scaffolds through upregulating ALP & BGLAP expression in hMSC-monocyte co-culture, *Biomater. Adv.*, 2023, **154**, 213622.
17 M. Razali, N. Ismail, U. Osman and K. Amin, Mechanical and Physical Properties of Gellan Gum (GG) Biofilm: Effect of Glycerol, *ASM Sci. J.*, 2018, **1**, 158–165.
18 . Preparation of gellan gum (GG) film: the effect of GG, calcium chloride ($CaCl_2$), glycerol concentration and heat treatment, in *IOP Conference Series: Materials Science and Engineering*, ed. N. A. Ismail, K. A. M. Amin and M. H. Razali, IOP Publishing, 2018.
19 C. Rong, T. Su, Z. Li, T. Chu, M. Zhu, Y. Yan, *et al.*, Elastic properties and tensile strength of 2D Ti3C2Tx MXene monolayers, *Nat. Commun.*, 2024, **15**(1), 1566.
20 B. Majhy, P. Priyadarshini and A. Sen, Effect of surface energy and roughness on cell adhesion and growth–facile surface modification for enhanced cell culture, *RSC Adv.*, 2021, **11**(25), 15467–15476.
21 B. Özcolak, B. Erenay, S. Odabaş, K. D. Jandt and B. Garipcan, Effects of bone surface topography and chemistry on macrophage polarization, *Sci. Rep.*, 2024, **14**(1), 12721.
22 H. Zhao, Q. Fu, Z. Wang, Z. Wang, J. Hu and J. Wang, Fabrication and characterization of bifunctional PCL/chitosan scaffolds decorated with MXene nanoflakes for bone tissue engineering, *Polymer*, 2024, **303**, 127111.
23 Y. He, Z. Deng, Y.-J. Wang, Y. Zhao and L. Chen, Polysaccharide/Ti3C2Tx MXene adhesive hydrogels with self-healing ability for multifunctional and sensitive sensors, *Carbohydr. Polym.*, 2022, **291**, 119572.
24 T.-Q. Zhou, X.-C. Wang, L.-Y. Gao, J.-N. Yan and H.-T. Wu, Construction and properties of curdlan gum/gellan gum binary composite gel system, *Food Hydrocolloids*, 2024, **148**, 109391.

25 J. Wei, L. Dai, X. Xi, Z. Chen, M. Zhu, C. Dong, *et al.*, Robust, ultrathin and flexible electromagnetic interference shielding paper designed with all-polysaccharide hydrogel and MXene, *Carbohydr. Polym.*, 2024, **323**, 121447.
26 S. N. Banitaba, D. Semnani, E. Heydari-Soureshjani, B. Rezaei and A. A. Ensafi, Nanofibrous poly (ethylene oxide)–based structures incorporated with multi–walled carbon nanotube and graphene oxide as all–solid–state electrolytes for lithium ion batteries, *Polym. Int.*, 2019, **68**(10), 1787–1794.
27 M. Shayan Asenjan, M. Asl Farshbaf, M. Razavi Aghjeh, A. Tavakoli and M. Rezaei, Synthesis of High-Strength TPU/MXene Nanocomposites via an In Situ Polymerization Method, *Macromolecules*, 2024, **57**(9), 3993–4006.
28 J. D. da Silva, D. C. Moreira and G. Ribatski, Chapter Four – An overview on the role of wettability and wickability as a tool for enhancing pool boiling heat transfer, in *Advances in Heat Transfer*, ed. J.P Abraham, J.M Gorman and W. Minkowycz, Elsevier, 2021, vol. 53, pp. 187–248.
29 M. A. Quetzeri-Santiago, A. A. Castrejón-Pita and J. R. Castrejón-Pita, The Effect of Surface Roughness on the Contact Line and Splashing Dynamics of Impacting Droplets, *Sci. Rep.*, 2019, **9**(1), 15030.
30 F. Han, M. Liu, F. Hu, Y. Zhao and Y. Peng, Spreading Behavior and Wetting Characteristics of Anionic Surfactant Droplets Impacting Bituminous Coal, *ACS Omega*, 2022, **7**(50), 46241–46249.
31 K. Zukiene, G. Monastyreckis, S. Kilikevicius, M. Procházka, M. Micusik, M. Omastová, *et al.*, Wettability of MXene and its interfacial adhesion with epoxy resin, *Mater. Chem. Phys.*, 2021, **257**, 123820.
32 R. Rakhmanov, S. Ippolito, M. Downes, A. Inman, J. AlHourani, J. Fitzpatrick, *et al.*, Influence of MXene Interlayer Spacing on the Interaction with Microwave Radiation, *Adv. Funct. Mater.*, 2024, 2410591.
33 P. Machata, M. Hofbauerová, Y. Soyka, A. Stepura, D. Truchan, Y. Halahovets, *et al.*, Wettability of MXene films, *J. Colloid Interface Sci.*, 2022, **622**, 759–768.
34 H. Zhou, F. Wang, Y. Wang, C. Li, C. Shi, Y. Liu, *et al.*, Study on contact angles and surface energy of MXene films, *RSC Adv.*, 2021, **11**(10), 5512–5520.
35 S. Marecik, I. Pudełko-Prażuch, M. Balasubramanian, S. M. Ganesan, S. Chatterjee, K. Pielichowska, *et al.*, Effect of the Addition of Inorganic Fillers on the Properties of Degradable Polymeric Blends for Bone Tissue Engineering, *Molecules*, 2024, **29**(16), 3826.
36 Y.-J. Wan, X.-M. Li, P.-L. Zhu, R. Sun, C.-P. Wong and W.-H. Liao, Lightweight, flexible MXene/polymer film with simultaneously excellent mechanical property and high-performance electromagnetic interference shielding, *Composites, Part A*, 2020, **130**, 105764.
37 S. Khademolqorani, H. Tavanai and F. Ajalloueian, Mechanical properties of silk plain–weft knitted scaffolds for bladder tissue engineering applications, *Polym. Adv. Technol.*, 2021, **32**(6), 2367–2377.
38 P. Zhang, X.-J. Yang, P. Li, Y. Zhao and Q. J. Niu, Fabrication of novel MXene (Ti 3 C 2)/polyacrylamide nanocomposite hydrogels with enhanced mechanical and drug release properties, *Soft Matter*, 2020, **16**(1), 162–169.
39 X. Qin, S. Lei, K. Yang, W. Xie and J. Wang, Green synthetic sodium alginate-glycerol-MXene nanocomposite membrane with excellent flexibility and mineralization ability for guided bone regeneration, *J. Mech. Behav. Biomed. Mater.*, 2024, **150**, 106336.
40 L. Ponsonnet, K. Reybier, N. Jaffrezic, V. Comte, C. Lagneau, M. Lissac, *et al.*, Relationship between surface properties (roughness, wettability) of titanium and titanium alloys and cell behaviour, *Mater. Sci. Eng., C*, 2003, **23**(4), 551–560.
41 G. P. Lim, C. F. Soon, A. M. Jastrzębska, N. L. Ma, A. R. Wojciechowska, A. Szuplewska, *et al.*, Synthesis, characterization and biophysical evaluation of the 2D Ti2CTx MXene using 3D spheroid-type cultures, *Ceram. Int.*, 2021, **47**(16), 22567–22577.
42 J. D. Orlando, L. Li, T. B. Limbu, C. Deng, M. E. Wolf, W. M. Vickery, *et al.*, Calcium phosphate graphene and Ti3C2Tx MXene scaffolds with osteogenic and antibacterial properties, *J. Biomed. Mater. Res., Part B*, 2024, **112**(6), e35434.
43 N. Srivastava and A. R. Choudhury, Thermo-reversible self-assembled novel gellan gum hydrogels containing amino acid biogelators with antibacterial activity, *Carbohydr. Polym.*, 2024, **324**, 121462.
44 R. Álvarez-Chimal, V. I. García-Pérez, M. A. Álvarez-Pérez, R. Tavera-Hernández, L. Reyes-Carmona, M. Martínez-Hernández, *et al.*, Influence of the particle size on the antibacterial activity of green synthesized zinc oxide nanoparticles using Dysphania ambrosioides extract, supported by molecular docking analysis, *Arabian J. Chem.*, 2022, **15**(6), 103804.
45 P. Kushram and S. Bose, Improving Biological Performance of 3D-Printed Scaffolds with Garlic-Extract Nanoemulsions, *ACS Appl. Mater. Interfaces*, 2024, **16**(37), 48955–48968.
46 A. Samourides, L. Browning, V. Hearnden and B. Chen, The effect of porous structure on the cell proliferation, tissue ingrowth and angiogenic properties of poly(glycerol sebacate urethane) scaffolds, *Mater. Sci. Eng., C*, 2020, **108**, 110384.
47 H.-H. Sun, J.-C. Wang, X.-M. Feng, S.-L. Zhu and J. Cai, Allicin Inhibits Proliferation and Promotes Apoptosis of Human Epidural Scar Fibroblasts, *World Neurosurg.*, 2020, **136**, e460–e4e8.
48 B. Özkahraman, Z. Özbaş, G. Bayrak, E. Tamahkar, I. Perçin, A. Kılıç Süloğlu, *et al.*, Characterization and antibacterial activity of gelatin–gellan gum bilayer wound dressing, *Int. J. Polym. Mater. Polym. Biomater.*, 2022, **71**(16), 1240–1251.
49 M. Abidullah, P. Jadhav, S. S. Sujan, A. G. Shrimanikandan, C. R. Reddy and R. K. Wasan, Potential Antibacterial Efficacy of Garlic Extract on Staphylococcus aureus, Escherichia coli, and Klebsiella pneumoniae: An In vitro Study, *J. Pharm. BioAllied Sci.*, 2021, **13**(Suppl 1), S590–S594.

